43th Fluid Dynamics Conference and Exhibit
10-13 January, 2005/ Reno, NV.

AIAA-2005-1280

Study of Tip-Vortex Formation Using Large-Eddy Simulation

Reza Ghias*, Rajat Mittal†, Haibo Dong‡
Department of Mechanical and Aerospace Engineering
The George Washington University, Washington, DC 20052,

and

Thomas S. Lund§
Department of Aerospace Engineering Sciences
The University of Colorado at Boulder, Boulder, CO 80309-0429

The formation of the tip-vortex from a rectangular NACA 2415 wing-tip at a chord Reynolds number of 10000 has been simulated. The simulations employ a parallelized compressible large-eddy simulation (LES) solver that has been developed to simulate wing and rotor tip-flows. The solver employs an immersed-boundary technique in conjunction with a curvilinear structured grid and the dynamic model is used to model the subgrid-scale (SGS) stress terms. A detailed discussion of the tip-vortex formation and evolution in the near wake is presented.

I. Introduction

THE blade-tip vortex is an important aerodynamic feature of the helicopter rotor wake due to its ability to impact the blade performance and cause undesirable noise and vibrations. An understanding of tip-vortex formation and evolution is a necessary precursor to developing blade-tip designs that can diminish these undesirable characteristics of the tip vortex. This has been the primary motivation for many of the experimental investigations of the rotor tip vortex that have been undertaken. [1-9]

Accurate numerical simulation of tip-flow is a difficult proposition. Turbulent diffusion and dissipation have a significant effect on the size and intensity of the tip-vortex and have to be modeled with reasonable accuracy.[10] Most of the numerical simulations in the past have employed dissipative schemes in conjunction with relatively coarse meshes, which cause inaccurate prediction of the size, location and strength of the tip-vortex. Furthermore, the flow in the tip vortex is highly unsteady, three-dimensional and non-homogeneous and contains a wide range of spatial and temporal scales. Thus, simple Reynolds Averaged-Navier-Stokes (RANS) approaches which are designed to solve for the steady state, time-averaged velocity and pressure field[11,12], are not expected to perform well in predicting this flow.

Large-eddy simulation, with the dynamic subgrid-scale model[13,14] is an approach which is well suited for this type of flow problem. The LES methodology falls somewhere between the Direct Numerical Simulation (DNS) and RANS[10] approaches. In LES the large energy-containing scales are resolved and only outcome of the small, unresolved (subgrid) scales is modeled. Dynamic SGS modeling is an approach in which a procedure for dynamically calculating the model constant is added on to the SGS model.[14,15] As the calculation proceeds, the dynamic procedure utilizes information from the smallest resolved scales to predict the energy transfer to subgrid-scales. The model constant is then computed from the estimated rate of energy transfer. The dynamic model is ideally suited for complex flows, since it automatically detects laminar regions and turns itself off. This modeling technique has been used successfully to simulate a variety of flows.[14,16-19] Moreover, LES provides detailed time-dependent information about the important large scale features of the flow field without the immense cost of a DNS which would resolve all the scales down to dissipation range.

---

* Graduate Research Assistant, Student Member AIAA
† Associate Professor, Senior Member AIAA.
‡ Research Scientist, Member AIAA.
§ Visiting Professor, Member AIAA.

In the current effort, we have used a LES solver to simulate a compressible wing-tip flow. The simulations are motivated by the experiments of Martin[20] and Martin *et al.*[21], where a rectangular one-blade rotor with a NACA 2415 section was employed. The blade had a tip radius of 406 mm and a 44.5 mm chord, and was balanced by a counterweight. The rotational frequency was set to 35.0 Hz (Ω = 70p rad/sec). This led to a rotor-tip speed of 89.28 m/s which corresponds to a tip Mach number and chord Reynolds number of 0.26 and 272,000 respectively. All the tests were conducted for an effective blade loading of C_T/s = 0.064 using a collective pitch of 4.5° where C_T and s are rotor thrust coefficient and rotor solidity respectively. High resolution three-dimensional velocity field measurement and flow visualization in the rotor-tip vortex were obtained using Laser Doppler Velocimetry (LDV).

In the current paper we will describe the simulation of a non-rotating blade at a tip Reynolds number of 100000. The focus of the paper is on examining the flow structure in the formation region of the tip-vortex as well as the evolution of the vortex in the near wake.

II. Numerical Methodology

A. Governing Equations

The governing equations are unsteady, viscous, compressible Navier-Stokes equations written in terms of conservative variables. The continuity, momentum and energy equations are:

$$\frac{\partial}{\partial t}\bar{r} + \frac{\partial}{\partial x_k}\left(\overline{r u_k}\right) = 0$$

$$\frac{\partial}{\partial t}\left(\overline{r u_i}\right) + \frac{\partial}{\partial x_k}\left(\overline{r u_k}\,\bar{u}_k + \bar{p}\,d_{ik} - \bar{s}_{ik} + t_{ik}\right) = F_i^{\Omega}$$

$$\frac{\partial}{\partial t}\bar{e} + \frac{\partial}{\partial x_k}\left[\bar{u}_k(\bar{e}+\bar{p}) - \bar{s}_{ik}\bar{u}_i + \overline{Q}_k + \bar{q}_k\right] = 0$$

where, the molecular heat flux and stress tensors are given by

$$Q_k = -\frac{g}{(g-1)\,\mathrm{Re}\,\mathrm{Pr}}\frac{\partial T}{\partial x_k} \quad \text{and}$$

$$s_{ik} = \frac{1}{\mathrm{Re}}\left(\frac{\partial u_i}{\partial x_k} + \frac{\partial u_k}{\partial x_i}\right) - \frac{2}{3}\frac{1}{\mathrm{Re}}d_{ik}\frac{\partial u_j}{\partial x_j}$$

respectively and F_i^{Ω} is the force associated with rotation. In the above equations, Pr is the Prandtl number and Re is the Reynolds number. The velocity components and the pressure are related to the total energy per unit volume through the equation of state for a perfect gas by

$$e = \frac{p}{(g-1)} + \frac{1}{2}r\,u_k u_k$$

The bar in the above equations indicates the resolved quantities, i.e. those scales that are represented on the given mesh. Furthermore, in the above equations, t and q are the subgrid-scale stress and heat flux respectively which are defined as:

$$t_{ik} = \overline{r\,u_k\,u_i} - \frac{\overline{r\,u_i}}{\bar{r}}\,\overline{r\,u_k}$$

$$q_k = \overline{p\,u_k} - \frac{\overline{r\,u_k}}{\bar{r}}\,\bar{p}$$

B. Sub-grid Scale Model

Closure in the above equations is provided by modeling the SGS stress and heat flux terms. A trace-free Smagorinsky model[22] is used for modeling the SGS stress and Yoshizawa's[23] model is used for parameterization of SGS energy (t_{kk}) wherein

$$t_{ij} - \frac{d_{ij}}{3} t_{kk} = -2C\bar{r}\,\Delta^2 \left|\bar{S}\right| \left(\overline{S_{ij}} - \frac{d_{ij}}{3} \overline{S_{kk}} \right)$$

$$t_{kk} = 2C_I\,\bar{r}\,\Delta^2 \left|\bar{S}\right|$$

In the above equations, ***S*** is the strain rate tensor, *?* is the grid spacing, C is the Smagorinsky's constant, and C_I is the SGS energy coefficient. The SGS heat flux is modeled as

$$q_k = -\bar{r}\,\frac{C\bar{r}\,\Delta^2 \left|\bar{S}\right|}{\mathrm{Pr}_t} \frac{\partial \bar{T}}{\partial x_k}$$

where Pr_t is the turbulent Prandtl number. The key feature of the dynamic model is that it provides a formula for calculating C, C_I and Pr_t directly from the resolved flow quantities. This procedure is explained by Moin et al. [14] and El-Hady et al.[18]for compressible flows. Since the tip-flow is completely inhomogeneous, the conventional dynamic model which relies on the presence of a homogeneous direction cannot be employed. There are two other implementations of the dynamic model which are suitable for fully inhomogeneous flow; the dynamic localization model of Ghosal *et al.*[24] and the Lagrangian dynamic model (LDM) of Meneveau *et al.*[25] The latter, which is computationally less expensive is used in our simulation. In this model, the Smagorinsky's coefficient is obtained by averaging along particle trajectories and therefore the implementation does not require the presence of a homogenous averaging direction.

C. Discretization of the Governing Equations

The equations are transformed to a generalized curvilinear coordinate system, while maintaining the strong conservation form of the equations[26]. The equations are discretized in this computational domain with a cell-centered arrangement using a hybrid second-order central-difference-QUICK scheme[27] which is introduced in the split fluxes[28]. The weight factor for each scheme can be adjusted and allows us to precisely control the numerical dissipation. The diagonal viscous terms are treated implicitly using a Crank-Nicolson scheme wherein all the other terms including the convective terms and cross-terms are treated explicitly using a low-storage, 3rd –order Runge-Kutta scheme.[29] Use of this mixed implicit-explicit scheme virtually eliminates the viscous stability constraint which can be quite severe in simulation of viscous flows. The resulting equations are solved by a LSOR iterative method.[26]

D. Mesh Topology and Immersed Boundary Method.

As shown by Mittal *et al.*[19], it is crucial that LES be coupled with non- or minimally dissipative numerical schemes such as the second-order central difference. A consequence of using non-dissipative schemes is that simulations become very sensitive to the quality of the mesh as aptly demonstrated.[30] Tip-flow simulations are usually carried out with a C-H type mesh[31] but this type of mesh has a four branch cuts where grid quality is usually quite poor. We have circumvented this issue by using the so-called "immersed boundary method (IBM)". The key feature of this method is that flow past immersed boundaries can be simulated on structured curvilinear grids that do not conform to the shape of the boundaries and this allows us to simulate this flow on a single-block mesh with no branch cuts. The use of this topologically simple grid allows us to maintain relatively better grid quality in the entire domain. In the current method, the geometry of immersed boundary is defined by a set of marker points. Cells whose centers lie inside the immersed body and have at least one neighboring cell whose cell-center lies outside the body, are marked as "ghost-cells". The rest of the cells with centers inside the body, which are not adjacent to immersed boundary, are marked as "solid" cells. Fig. 1 shows the marker points, fluid cells, ghost cells and solid cells for an immersed boundary on a Cartesian grid. The basic idea in this method is to compute the flow variables for the ghost cells such that boundary conditions on the immersed boundary in the vicinity of the ghost cell are satisfied.

The advantage of this approach for the current tip flow is that since the blade does not vary in shape across the span, we can simply use a planar mesh in the spanwise direction. This greatly simplifies the mesh topology and discretization and gives us much more precise control over the grid quality. The use of a curvilinear mesh still

allows us control over the grid resolution in localized regions such as boundary layers. Fig. 2 shows the grid of 460 x179 in *x-y* plane which is used for simulation of tip flow around a NACA 2415 airfoil. Since the surface of the airfoil is mostly parallel to one set of grid lines, this allows us to provide a higher resolution selectively in the boundary layer region. A similar approach has been used for incompressible tip-clearance flow simulations.[32] Accuracy tests and validation of this solver against established experiments and simulations has been described in detail in previous paper. [33]

E. Parallelization of the solver

An efficient and flexible Message-Passing Interface (MPI) based parallel version of the solver has been developed for the tip-flow simulations. In the algorithm adopted, the computational domain is decomposed into several sub-domains in the stream wise direction. Each sub-domain is enclosed with a layer of overlapping points. These overlapping points store flow variables transferred from the neighboring sub-domain for the solution of variables within the sub-domain. The key feature of the domain decomposition is the implementation of the LSOR iterative method that is used to solver the transport equations. The method currently adopted employs the Jacobi's iterative at the domain interfaces but retains a Gauss-Sidel approach for all the nodes inside a given domain. Tests indicate that the convergence properties of the iterative method do not deteriorate due to this procedure. Our parallel code has been successfully tested on an in-house 16-CPU Beowulf cluster which consists of 2.8 GHz Pentium-4 processors and employs a gigabit interconnect between the nodes. Extensive tests show that the parallel code achieves reasonably good parallel efficiency for grid sizes that are relevant for the tip-flow simulations.[35]

F. Tip-Flow Configuration

The flow configuration is schematically shown in Fig. 3. As mentioned before, the experimental configuration that we have chosen is the one that was the subject of the detailed study by Martin.[20] .The computational domain is of size L_x x L_y x L_z = 3.5*C* x 4.0*C* x 3.0*C*, where *C* is the chord length. The domain extends 1.0*C* upstream of the leading edge and 1.0*C* downstream of the trailing edge. This should allow us to capture the wake with age up to 5 degrees with enough resolution in the streamwise (*x*) direction. The vertical (*y*) extent of the domain is large enough to ensure that that the boundary layer grows naturally with minimum effect from the vertical boundary. The choice of the spanwise domain size is driven by the size of the tip-vortex and the fact that far enough from the tip of the airfoil there is not much variation in the spanwise *(z*) direction. Thus the spanwise domain size is extended to 1.0*C* and 2.0*C* on the inward and outward of the blade tip respectively. The simulation is performed in a reference-frame attached to the rotor which eliminates the need to incorporate a moving boundary in computation.

The flow is assumed to be compressible with constant specific heat ratio. At the inflow, all velocity components as well as the temperature are imposed, while the density is extrapolated from the domain and pressure is calculated by using the equation of state. At the outflow, a non-reflecting Navier-Stokes characteristic boundary condition[29] is used which allows vortex structures to exit the computational domain with minimal spurious reflections. The lateral boundaries are treated as moving walls, and density and temperature are determined by assuming adiabatic wall condition. The no-slip boundary condition is imposed at the surface of circular cylinder. Zero-stress boundary conditions at the inner spanwise boundary and free stream conditions are imposed at the outer spanwise boundary.

III. Numerical Results and Discussion

A. Non-rotational tip-flow simulations

In the current paper we describe the results from simulations where the rotation effects have not been included. This is a precursor to simulations where all of the rotational effects will be accounted for. Also, the current simulations have been carried out at a Reynolds number of 100000. The grid requirements for a simulation at the experimental Reynolds number currently put it outside our reach. It is however felt that the Reynolds number of 100000 is high enough that the essential features of the flow will be similar to that observed at the higher Reynolds number. It should be noted that the mesh used in the current simulation has over twelve million mesh points and requires almost 20,000 single-node CPU hours on a 2.8 GHz Pentium-4 per chord-flow time. The Mach number of 0.26 matches the experiment.

Fig. 4 shows an iso-surface of streamwise vorticity at one time instant and this gives a clear view of the three-dimensional vortex topology in the formation region. The plot clearly shows the presence of at least two strong vortex systems, one associated with the suction side of the wing and the other from the pressure side of the wing-tip. In order to examine the vortex structure in more detail, in Fig. 5a we have plotted contours of streamwise vorticity at a number of streamwise stations along the wingtip. Near the leading edge we observe the formation of two counter rotating vortices which are formed due to the leakage of flow from the wing surface to the tip region. This is due to

the strong spanwise pressure gradient that is known to be present in this region.[1,4,36,37] We denote the vortex from the suction surface as vortex-A and that from the pressure surface as vortex-B. At x/c =0.1-0.2, these two vortices are observed to be of almost equal strength and have nearly circular vortex cores. At x/c=0.3 we observe the development of a new vortex feature on the suction surface. This station is located where the pressure on the suction side wing surface is lower than that in the tip region. This results in the flow turning from the wing tip region back onto the suction surface. This has two consequences; first vortex-A also convects toward the suction surface and second, a new vortex (vortex-C) is created due to the rollup of the shear layer that forms as a result of the flow moving from the tip to the suction surface. Vortex-C has a rotation opposite to that of vortex-A and in fact vortex-C is the primary wing tip vortex. At x/c=0.4, as vortex-C grows, it tends to wrap vortex-A around itself. At the same time, vortex-A starts to lose strength due to cross diffusion of vorticity with vortex-C. At this station we also see that due to the bulk flow from the wing-tip to the suction surface, vortex-B also starts to convect upwards. By the time the vortices reach at x/c =0.9, vortex-C has gained significantly in strength whereas vortex-A has all but disappeared. Furthermore, vortex-B has reached the suction surface and is beginning to interact with the wing-tip vortex-C. In fact, we observe that at this plane, vortex-B creates a set of small tertiary vortex structures on the suction surface. At x/c=1.0 which is at the trailing edge, the wing tip vortex-C is the dominant feature in the flow and moved significantly inwards away from the tip region. Thus, at this relatively low Reynolds number, secondary vortices play a significantly role in the formation of the wing-tip vortex. It is known that the effect of these secondary vortices diminishes at higher Reynolds numbers [2,3].

Fig. 5(b) shows streamwise vorticity at a number of streamwise planes in the near wake. It can be observed that in very near wake, secondary and tertiary vortices continue to interact with the primary wing-tip vortex and modify its structure. Figs. 6(a-c) show the cross-plane velocity vectors at several streamwise locations beyond the trailing edge and Figs. 6(d-f), show the corresponding vorticity vectors. The vorticity vector field shows that a significant amount of cross stream vorticity comes from the shear layer formed at the trailing edge of the wing and rolls up into a spiral structure. The secondary and tertiary vortices also clearly affect the accumulation of vorticity inside the primary vortex.

Fig. 7 shows the spanwise variation of the absolute value of the cross-plane component of velocity at various streamwise stations in the near wake cutting through the primary vortex core. Note that the wing tip is located at z/R=1. The distance between the two maximas in these velocity profiles is indicative of the vortex core size. The plot shows that the magnitude of the cross velocity and core size decreases monotonically in the downstream direction. Fig. 8 shows the vertical component of velocity profiles at these locations. This velocity is observed to also reduce in magnitude as we move downstream and this is symptomatic of the effect of the accelerated viscous diffusion.[39] It is also clear that there is a strong asymmetry in the velocity profile. Fig. 9 shows the streamwise velocity in the core of the tip-vortex at different cross-plane locations. The region of the streamwise velocity deficit is much broader than the region of swirl velocity which in agreement with experimental measurements.[15,38,40] Figs. 10(a,b) show that tip vortex centerline position in various streamwise planes starting from the trailing edge of the airfoil. It is clear that the tip vortex moves downward and inboard in y (vertical), and z (spanwise) directions.

Simulations with rotational effects included are currently being carried out and these results will be presented in the future.

Acknowledgement

This research is supported by the U.S. Army Research Office Grant No. DAAD19-01-1-0704, monitored by Dr. T. Doligalski.

References

[1]Francis, M. S., and Kennedy, D.A., " Formation of a Trailing Vortex," Journal of Aircraft, Vol. 16, No. 3, 1979, pp. 148-154.

[2]Li, H., Burggraf, O. R., and Conlisk, A. T., " Formation of a Rotor Tip Vortex," Journal of Aircraft, Vol. 39, No. 5, 2002, pp. 739-749.

[3]Brich, D., Lee, T., Mokhtarian, F. and Kafyeke, F., " Rollup and Near-Field Behavior of a Tip Vortex," Journal of Aircraft, Vol. 40, No. 3, 2003, pp. 603-607.

[4]Chow, J. S., Zilliac G. G., and Bradshaw, P., "Mean and Turbulence Measurements in the Near Field of a Wingtip Vortex," *AIAA J.*, Vol. 35, No. 10, (1997), pp 1562-1567.

[5]Shekarriz, A., Fu, T. C., Katz, J., and Huang, T. T., " Near Field Behavior of a Tip Vortex," *AIAA J.*, Vol. 31, No. 1, (1993), pp. 112-1118.

[6]Lishman, J.G. and Bagai, A., Challenges in Understanding the Vortex Dynamics of Helicopter Rotor Wakes. *AIAA J.* 36, No. 7 (1998) 1130-1140.

[7]Bhagwat, MJ, and Leishman, J.G., Correlation of Helicopter Rotor Tip Vortex Measurements., *AIAA J.*, Vol. 38, No. 2(2000) 301-308

[7]McAlister, KW, Schuler, CA, Brannum, L., and Wu, Jc. 3-D wake Measurements Near a Hovering Rotor for Determining Profile and Induced Drag. NASATP 3577(1995).

[9]Thompson, Tl, Komerath, NM and Gray, RB, Visualization and Measurement of the Tip Vortex Core of Rotor Blade in Hover, J. Aircraft, Vol. 25, No.12(1988) 1113-1121.

[10]Srinivasan, G.R. and McCroskey, W.J., " Navier-Stokes Calculations of Hovering Rotor Flow Fields," *J. Aircraft*, Vol. 25, No. 10, (1988), pp. 865-874.

[11]Wake, B.E. and Sankar, L.N., "Solutions of the Navier-Stokes Equations for Flow About a Rotor Blade," *J. Am. Hel. Soc.*, 34(2), (1989), pp. 13-23.

[12]Srinivasan, G.R., Baeder, J.D., Obayashi, S, and McCroskey, W.J., "Flow field of a Lifting Rotor in Hover: A Navier-Stokes Simulation," *AIAA J.*, Vol. 30, No. 10, (1992), pp 2371-78.

[13]Germano, M., Piomelli, U., Moin, P., and Cabot, W., " A Dynamic Subgrid-Scale Eddy-Viscosity Model," Phys. of Fluids, A3, (1991), pp. 1760-65.

[14]Moin, P., Squires, K., Cabot, W., and Lee, S., " A Dynamic Subgrid-Scale Model for Compressible Turbulence and Scalar Transport," Phys. of Fluids, A3 (11), (1991), pp. 2746-57.

[15]Rogallo, R.S. and Moin, P., "Numerical Simulations of Turbulent Flows," Annu. Rev. Fluid Mech., 16, (1984), pp.99-137.

[16]Beaudan, P., and Moin, P., Numerical experiments on the flow past a circular cylinder at sub-critical Reynolds number., report No. TF-62, Thermo-sciences Division, Department of Mechanical Engineering, Stanford University, (1994).

[17]Kaltenbach, H.J., Fatica, M., Mittal, R., Lund, T.S., and Moin., P., " Study of Flow in an Asymmetric Planar Diffuser Using Large-Eddy Simulation," J. Fluid Mech., 390, (1999), pp. 151-185.

[18]El-Hady, N.M., " Large-Eddy Simulation of Laminar-Turbulent Breakdown at High Speed with Dynamic Subgrid-Scale Modeling," NASA CR 4533., (1993).

[19]Mittal, R., Moin, P., "Suitability of Upwind-Biased Schemes for Large-Eddy Simulation of Turbulent Flows," *AIAA J.*, Vol. 36, No. 8, (1997), pp. 1415-17.

[20]Martin, B. P., "Measurements of The Trailing Vortex Formation, Structure, and Evolutionin The Wake of Hovering Rotor", Doctoral Dissertation, University of Maryland.(2001)

[21]Martin, BP, Pugliese, GJ, and Lieshman , GJ, High Resolution Trailing Vortex Measurements in The Wake of a Hovering Rotor., American Helicopter Society, 57th Annual Forum, Washington, DC, May 9-11(2001).

[22]Erlebacher, G., Hussaini, M.Y., Speziale, C.G., and Zang, T.A., "Towards Large-Eddy Simulations of Compressible Turbulent Flows," J. Fluid Mech., 238, (1992), pp. 155-185.

[23]Yoshizawa, A., "Statistical Theory for Compressible Turbulent Shear Flows with the Application to Subgrid Modeling," Phys. Fluids, 29, (1986), pp. 2152.

[24]Ghosal, S., Lund, T.S., Akselvoll, K., and Moin, P.,"A Dynamic Localization Model for Large-Eddy Simulation of Turbulent Flows," J. Fluid Mech., Vol. 286, (1995), pp. 229-255.

[25]Meneveau, C., Lund, T.S., and Cabot, W. H., "A Lagrangian Dynamic subgrid-Scale Model of Turbulence," J. Fluid Mech., 319, (1996), pp. 353-385.

[26]Anderson, A.D., Tannehill, C.J., and Pletcher, R.H., Computational Fluid Mechanics and Heat Transfer, Hemispher Publishing Corporation, New York, 1984, pp. 479-482.

[27]Leonard, B. P., "A stable and accurate on convection modeling procedure based on quadratic upstream interpolation," Computer Methods in Applied Mechanics and Engineering, 19, (1979), pp. 59-98.

[28]Steger, JL, and Warming, RF, "Flux Vector Splitting of Inviscid Gasdynamic Equations with Application to Finite-Difference Methods,"J. of Compu. Phys. No. 40, (1981), pp. 263-293.

[29]Kennedy, C. A., Carpenter, M. A., and Lewis, R. M., "Low-storage, explicit Runge-Kutta scheme for the compressible Navier-Stokes equations," ICASE Report No. 99-22,(1999).

[30]You, D., Wang, M., Mittal, R., Moin, P., **"**Study of rotor tip-clearance flow using large eddy simulation," *AIAA* (2003)-838

[31]Kunz, R. F., Lankshminarayana, B., and Basson, A. H., "Investigation of Tip Clearance Phenomena in an axial Compressor Cascade Using Euler and Navier-Stockes Procedures," ASME J. Turbomach., 115, (1993), pp. 453-467.

[32] You, D., Mittal. R., Wang, M., and Moin, P., "Computational Methodology For Large-Eddy Simulation of Tip-Clearance Flows," AIAA J., Vol. 42, No. 2, (2004), pp. 271-279.

[33]Ghias, R, Mittal, R, and Lund TS, "A Non-Body Conformal Grid Method for Simulation of Compressible Flow with Complex Immersed Boundaries," AIAA2004-0080, Jan. 2004, Reno, NV.

[34]Poinsot, T. J., and Lele, S. K.," Boundary Conditions for Direct Simulations of Compressible Viscous Flows," *J. Comput. Phys*., 101, (1992), pp. 104-129.

[35]Ghias, R, Mittal, R, Dong, H., and Lund, T. S., " Large-Eddy Simulation of the Tip Flow of a Rotor in Hover Flow," AIAA2004-0080, 28 June-1 July, 2004, Portland, OR.

[36]Bacon, D. L., " The Distribution of Lift over Wing Tips and Ailerons," NACA Report No. 161, 1924.

[37]Munk, M. M.," Note on Vortices and Their Relation to the Lift of Airfoil,." NACA TN 184, 1924.

[38]Ramparian, B. R., and Zheng, Y.," Measurements in Rollup Region of the Tip Vortex From a Rectangular Wing" *AIAA J.*, Vol. 35, No. 12, (1997), pp. 1837-43.
[39]Squire, H. B.," The Growth of a Vortex in Turbulent Flow," The Aeronautical Quarterly, August 1965, pp. 302-305.
[40]Shekarriz, A., Fu, T. C., and Katz, J., " Study of Junction and Tip Vortices Using Particle Displacement Velocimetry," *AIAA J.*, Vol. 30, No. 1, (1992), pp. 145-152.

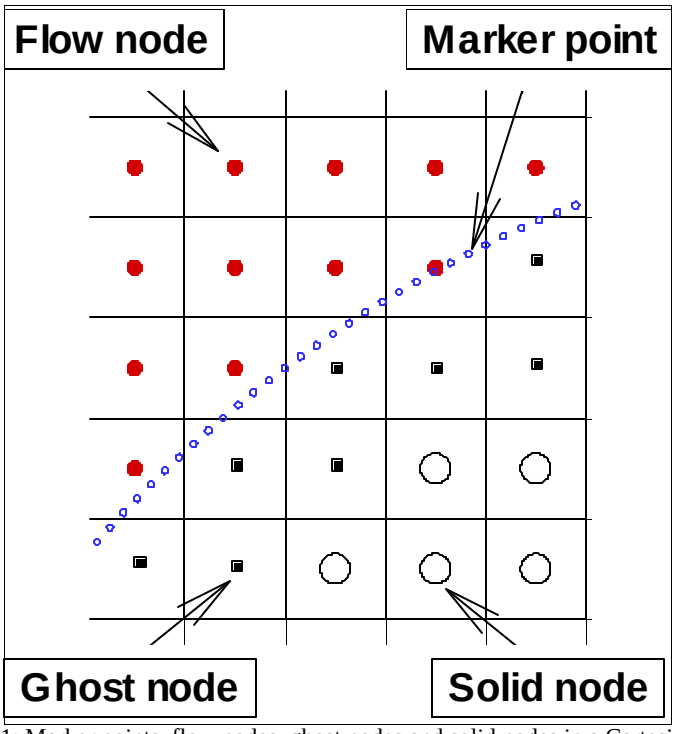

Figure 1: Marker points, flow nodes, ghost nodes and solid nodes in a Cartesian grid.

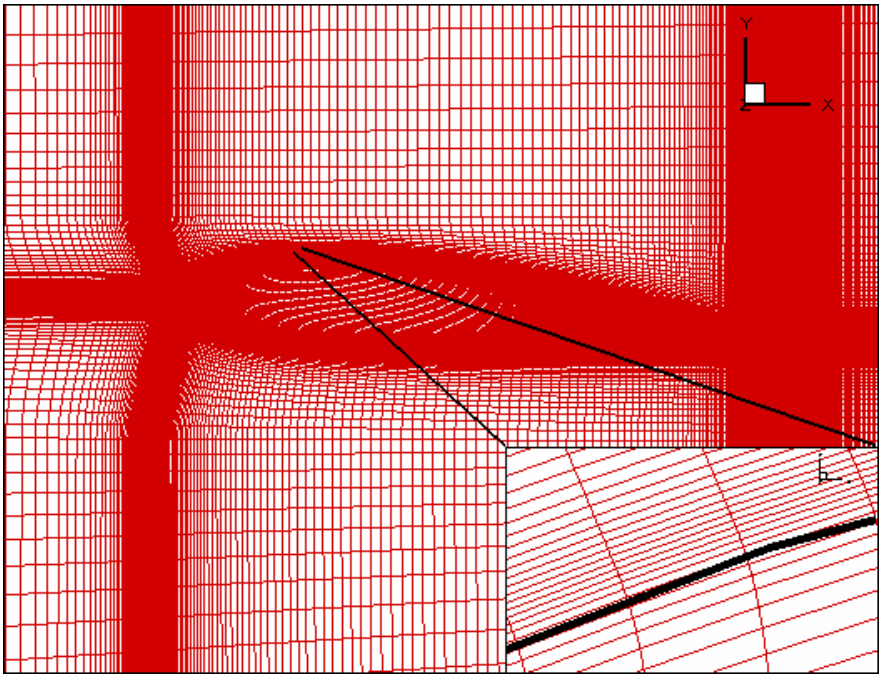

Figure 2: The rectangular curvilinear domain in x-y plane. Grid size is 460×197. The black line provides a rough indication of the location of the airfoil surface.

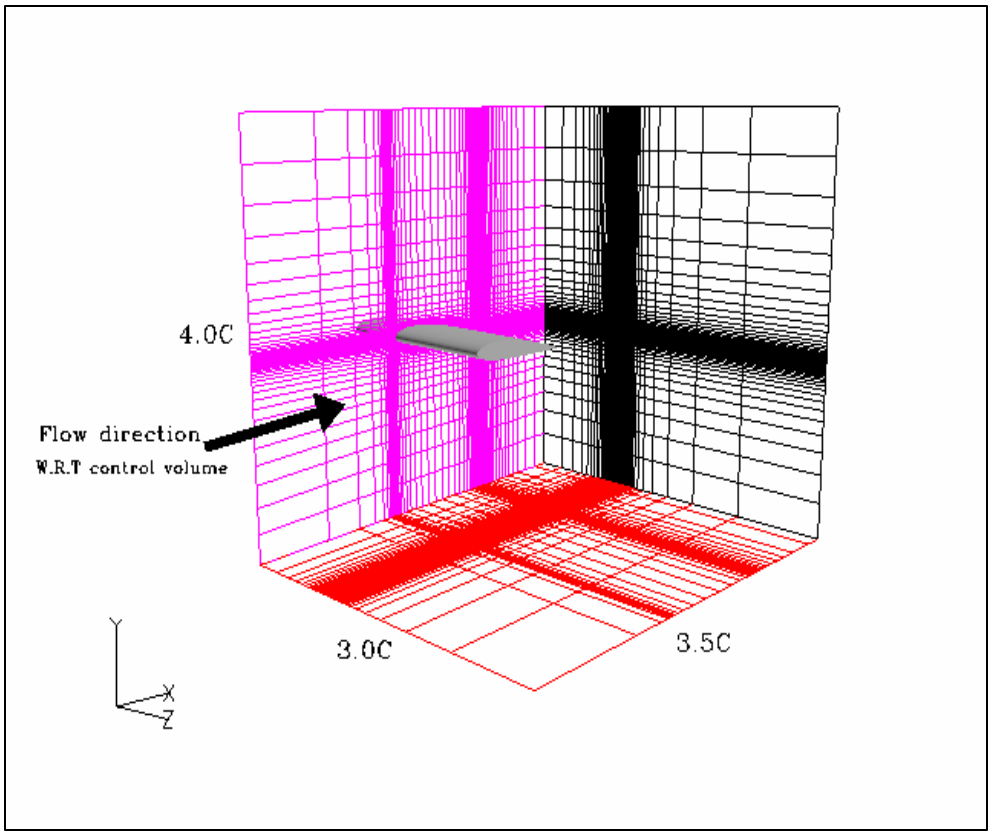

Figure 3: Flow configuration for simulation of tip-flow. The computational domain is L_x x L_y x L_z = 3.5C x 4.0C x 3.0C.

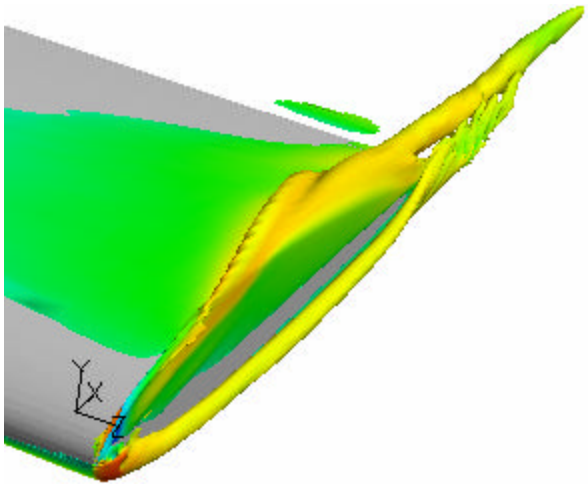

Figure 4: Iso-surface of streamwise vorticity in near field Re=100,000, M=0.26.

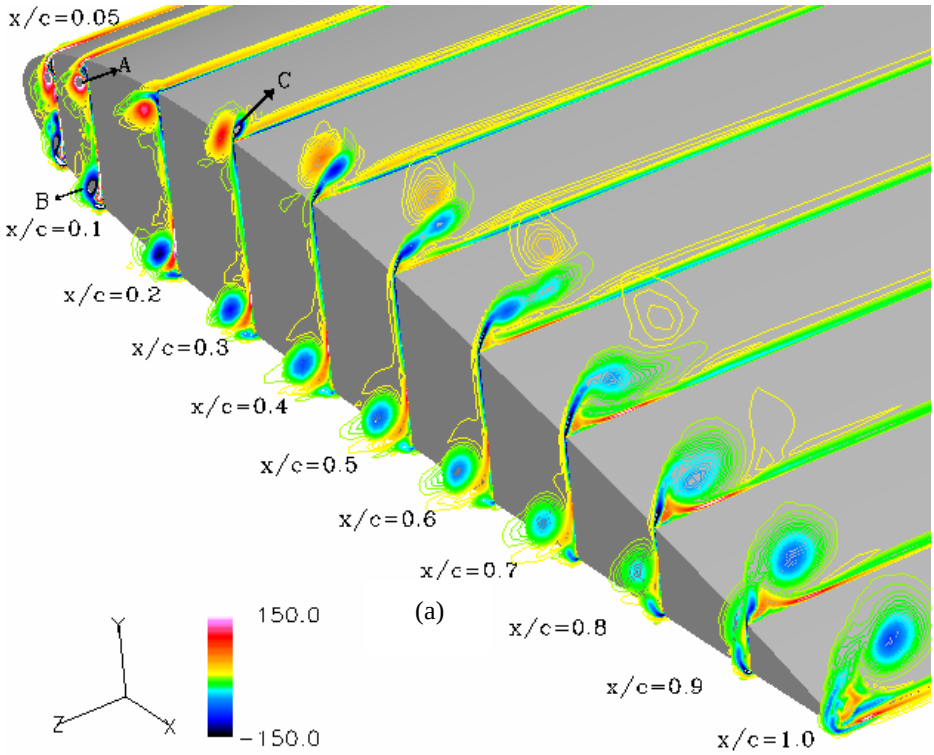

(a)

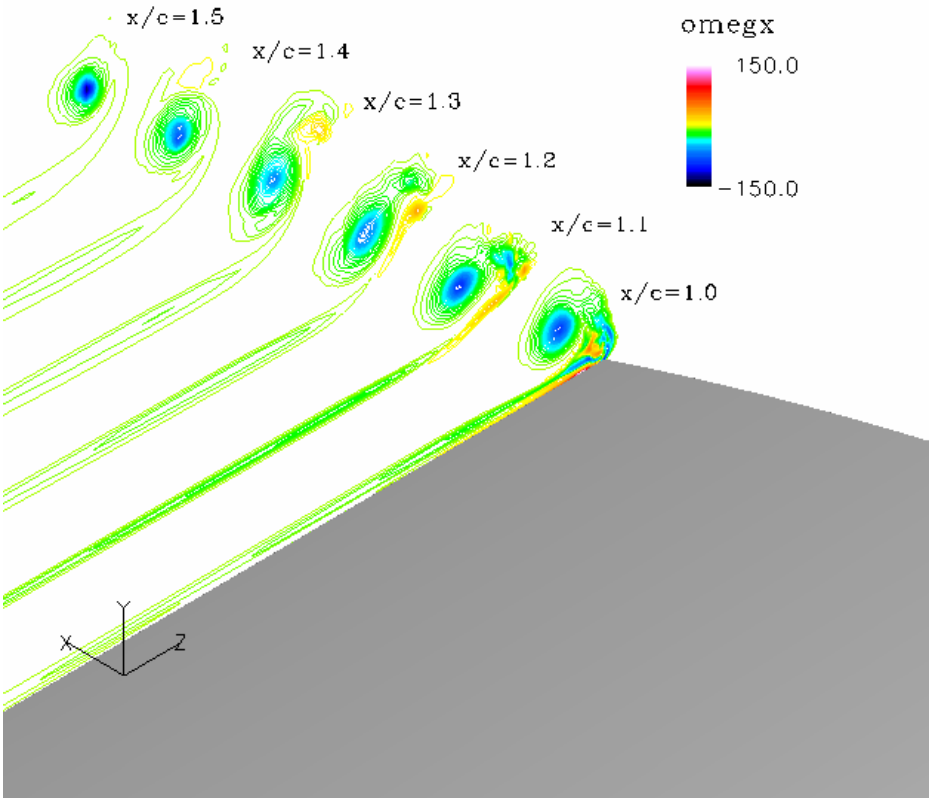

(b)

Figure 5: Contours of axial component of vorticity at various *x/c* for *Re*=100,000, and M=0.26 (a) wing tip region (b) near wake region.

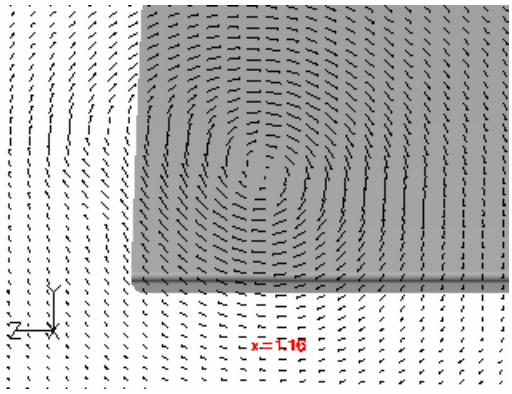

(a) x=1.16

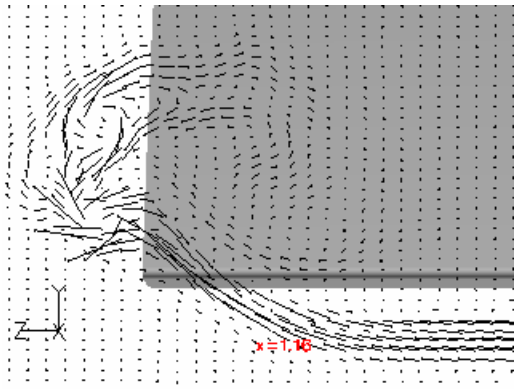

(d) x=1.16

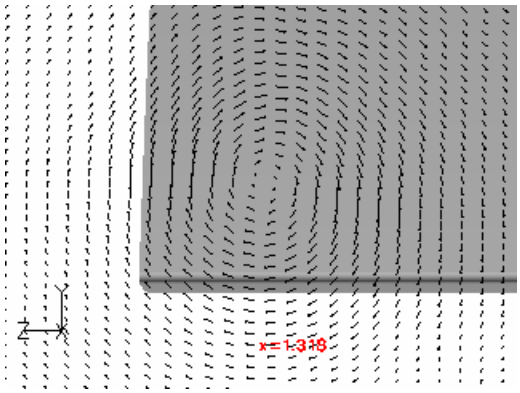

(b) x=1.318

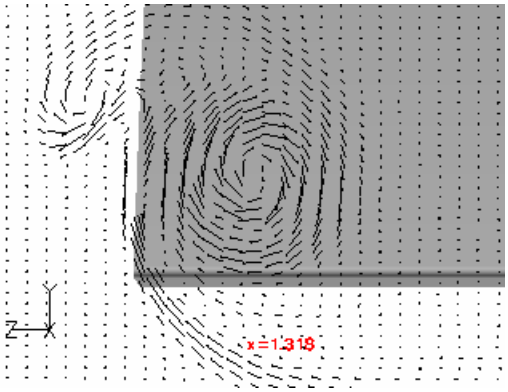

(e)x=1.318

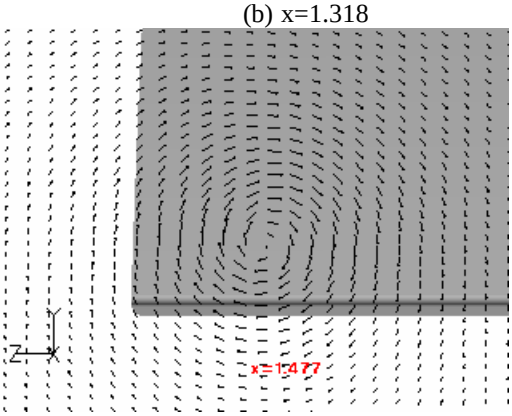

(c) x=1.477

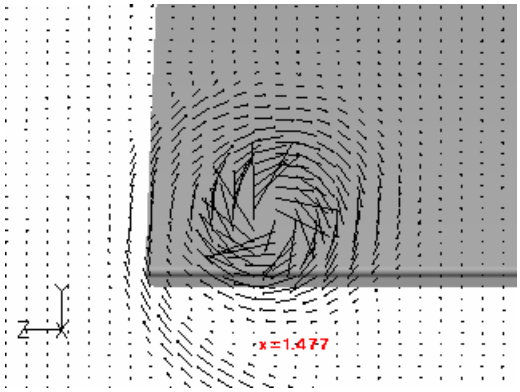

(f)x=1.477

Figure 6 :(a-c) Cross-plane vectors and, (d-f) and corresponding cross-vorticity vectors in the streamwise planes near wake region, Re=100,000, M=0.26.

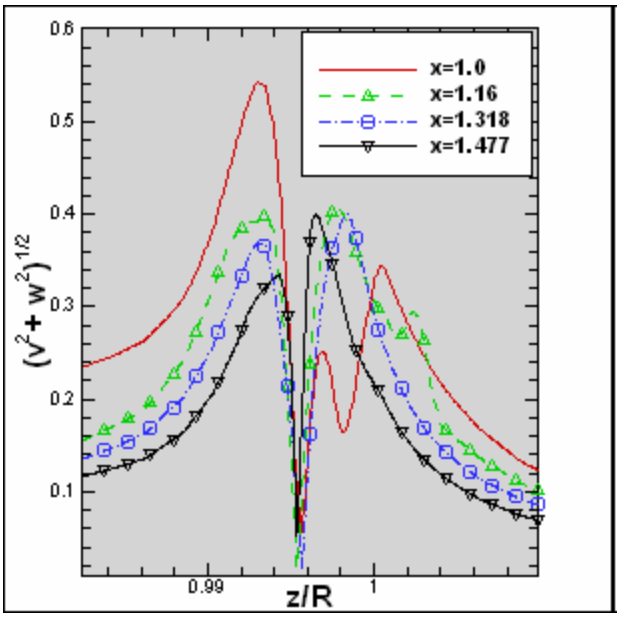

Figure7: cross-plane velocity magnitude in the core at different x locations

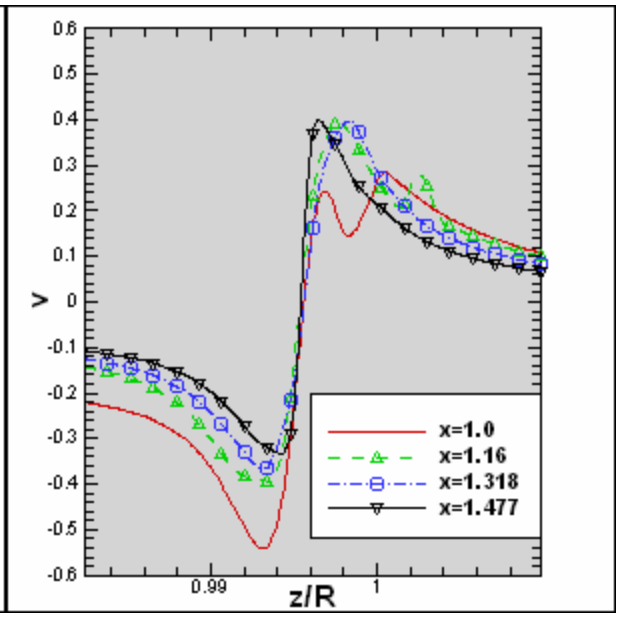

Figure8: Vertical component of velocity in the core core at different x locations

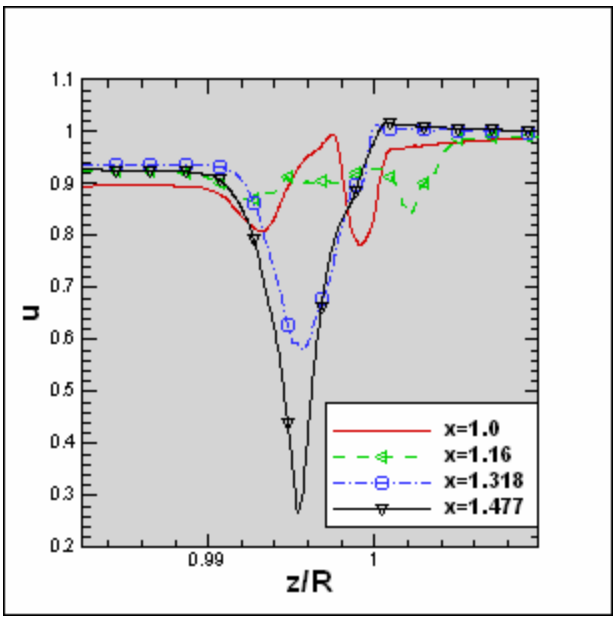

Figure9: streamwise velocity in the core at different x locations

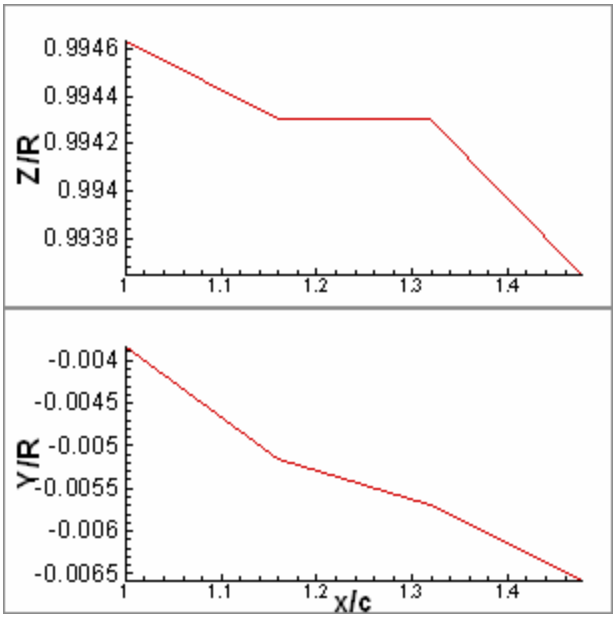

Figure10: location of the tip vortex centerline